

\bar{D} -meson Nucleon Scattering from Lattice QCD at the Physical Point

Wren Yamada,^{1,*} Yan Lyu,¹ Kotaro Murakami,^{2,1} and Takumi Doi¹

(HAL QCD collaboration)

¹*RIKEN Center for Interdisciplinary Theoretical and
Mathematical Sciences (iTHEMS), RIKEN, Wako 351-0198, Japan*

²*Department of Physics, Institute of Science Tokyo,
2-12-1 Ookayama, Meguro, Tokyo 152-8551, Japan*

(Dated: March 13, 2026)

arXiv:2603.12251v1 [hep-lat] 12 Mar 2026

Abstract

We report the first lattice QCD study of the s -wave scattering of the \bar{D} -meson and the nucleon at the physical point, utilizing (2+1)-flavor configurations generated by the HAL QCD collaboration with a pion mass of $m_\pi \simeq 137$ MeV and a lattice spacing of $a \simeq 0.084$ fm. By applying the HAL QCD method to the four-point correlation function of the $\bar{D}N$ system, we obtain a leading-order potential of the derivative expansion of the interaction kernel, which is then used to extract the s -wave phase shifts of low-energy $\bar{D}N$ scattering. Both the isospin $I = 0$ and $I = 1$ channels have a short-range repulsive core and a shallow attractive pocket in the intermediate to long-range region, though the $I = 0$ channel is more attractive than the $I = 1$ channel. We also observe that the $\bar{D}N$ potential exhibits more attraction than the KN potential, which is its analog in the strange sector. In terms of the s -wave phase shifts, the $I = 0$ channel shows a weak attractive behavior in the low-energy region with a positive scattering length of $0.246 \pm 0.105^{(+0.084)}_{(-0.051)}$ fm, whereas the $I = 1$ channel shows repulsion with a negative scattering length of $-0.086 \pm 0.050^{(+0.037)}_{(-0.001)}$ fm. No bound states are found in both isospin channels, indicating the absence of a pentaquark state in the s -wave $\bar{D}N$ system.

I. INTRODUCTION

The study of hadron-hadron interactions, including those involving charm, is vital in various aspects of hadron and nuclear physics. For example, it is important in understanding hadron resonances, especially exotic hadrons such as tetraquark or pentaquark states beyond conventional quark configurations (e.g., $X(3872)$, T_{cc} , P_c), situated near the two-body hadronic thresholds with charmed hadrons [1–11]. Also, interactions between charmed hadrons and nucleons give us insight into the spectrum of charmed nuclei, and in-medium modifications of mass and width of charmed hadrons in nuclear matter [12–19].

In this paper, we investigate the interaction between the \bar{D} meson and the nucleon (N) at low energies using first-principles lattice QCD calculations of the underlying theory of quantum chromodynamics (QCD). The $\bar{D}N$ system is the charm analog of the KN system, with a quark configuration of $\bar{c}qqqq$ ($q = u$ or d) with no quark-antiquark annihilation

* rento.yamada@riken.jp

of the valence quarks. Thus, the \bar{D} meson and the nucleon can form an explicitly exotic pentaquark state if the attraction between the two is strong enough to form a bound state. It is discussed in some literature [12, 20–23] that heavy-quark spin symmetry [24] plays an important role in yielding attraction between the \bar{D} meson and the nucleon. In contrary to the case of the kaon, the approximate degeneracy of the \bar{D} meson and the \bar{D}^* meson, with a mass difference of 140 MeV, is expected to enhance the coupling between the $\bar{D}N$ and \bar{D}^*N channels, effectively generating more attraction. There have been various theoretical studies using effective models to investigate the $\bar{D}N$ interaction [20–23, 25–28] that disagree qualitatively. While some theoretical models indicate a strong attraction between the \bar{D} meson and the nucleon sufficient to form bound states [20–23], other models only show weak attraction or repulsion. The scattering lengths also vary depending on the model likely due to the undetermined model parameters. From the experimental side, conventional two-body scattering experiments are incredibly challenging in the case of $\bar{D}N$ system. Femtoscopy analysis of the D^-p momentum correlation function from pp collisions by the ALICE collaboration [29] is the first experimental measurement concerning the two-body interaction between open charmed mesons and nucleons. Though present data do not yield a definitive conclusion on the low-energy scattering behavior of $\bar{D}N$, the LHC RUN-3 data with significantly larger statistics is expected to be available in the new future, which should improve our understanding of the $\bar{D}N$ system. Given these circumstances, we anticipate that a realistic lattice QCD investigation will play a critical role in both theoretical and experimental studies concerning the $\bar{D}N$ system at low energies.

The HAL QCD method [30–33] is one of the established ways to extract hadron-hadron interactions from lattice QCD simulations. While the Lüscher’s finite volume method [34, 35] extracts scattering information from the volume-dependence of the energy shifts in finite volume, the HAL QCD method extracts interaction information from the temporal and spatial profiles of the Nambu-Bethe-Salpeter (NBS) wave functions. Many studies of hadron-hadron interactions using the HAL QCD method have been conducted employing the configurations near the physical point with a pion mass of $m_\pi = 146$ MeV [36–43]. Now, it is possible to perform physical-point simulations using the new configurations generated by the HAL QCD collaboration with a physical pion mass of $m_\pi = 137$ MeV [44]. Employing this physical-point configuration, the $N\Omega_{ccc}$ system [45] and KN system [46]

have been studied recently. In this study, we investigate the $\bar{D}N$ system using the same configuration, and obtain the interaction potential, s -wave phase shifts, scattering length and effective range. Though this study is performed using a single-channel formalism, our calculation implicitly includes effects from the \bar{D}^*N channel, so that we obtain the correct phase shifts near the $\bar{D}N$ threshold. We note that this is the first investigation of the $\bar{D}N$ system from lattice QCD simulations.

The paper is organized as follows. In Sec. II, we introduce the time-dependent HAL QCD method applied to a meson-baryon system. We outline how to extract the potential and phase shifts from correlation functions. In Sec. III, details of the lattice simulation setup are presented. Then in Sections IV and V, the results of our HAL QCD analysis are given. In Sec. IV, we present the leading-order potentials in the derivative expansion of $\bar{D}N$ in the isospin $I = 0$ and $I = 1$ channels. We also compare the $\bar{D}N$ potentials to the KN potentials presented in Ref. [46]. In Sec. V, we present the s -wave phase shifts, scattering length and effective range of the $\bar{D}N$ system. Section VI concludes this paper.

II. HAL QCD METHOD

Here we summarize the HAL QCD method [30–33] to outline the procedure in obtaining the potentials and phase shifts of $\bar{D}N$ scattering from lattice QCD simulations. We will consider the general case of a scattering problem of a meson and a baryon.

First, consider the four-point correlation function

$$C_{4\text{pt}}^{MB}(\vec{r}, t) = \sum_{\vec{x}} \langle 0 | M(\vec{x} + \vec{r}, t) B(\vec{x}, t) \bar{\mathcal{J}}(0) | 0 \rangle, \quad (1)$$

where, M (B) represents the point-like sink operators for the meson (baryon) field, and operator $\bar{\mathcal{J}}(0)$ is a source operator placed at $t = 0$, overlapping with the meson-baryon two-body states. For sufficiently large t , $C_{4\text{pt}}^{MB}(\vec{r}, t)$ behaves as

$$C_{4\text{pt}}^{MB}(\vec{r}, t) = \sum_n a_n \psi_n(\vec{r}; E_n) e^{-\Delta E_n t} + \mathcal{O}(e^{-\Delta E^* t}), \quad (2)$$

where $\psi_n(\vec{r}; E_n)$ is the equal-time Nambu-Bethe-Salpeter (NBS) wave function and $a_n = \langle n | \bar{\mathcal{J}}(0) | 0 \rangle$ is the overlap of the source operator for the n -th eigen state of the meson-baryon system. ΔE_n is the eigen energy of the n -th eigen state and ΔE^* is the energy of the lowest inelastic scattering states, with respect to the two-body threshold at $E = m_M + m_B$. m_M

(m_B) corresponds to the mass of the meson (baryon). When considering sufficiently large time, contributions from the inelastic states are exponentially suppressed, and can be regarded as negligible.

Let us now define the R-correlator $R(\vec{r}, t)$ as

$$R(\vec{r}, t) = \frac{C_{4\text{pt}}^{MB}(\vec{r}, t)}{C_{2\text{pt}}^M(t) C_{2\text{pt}}^B(t)}, \quad (3)$$

where $C_{2\text{pt}}^{M(B)}(t)$ denotes the two-point correlation functions of the meson (baryon) operators at Euclidean-time t . As shown in Refs. [32, 47, 48], the R-correlator satisfies the following equation

$$\left[\frac{1 + 3\delta^2}{8\mu} \partial_t^2 - \partial_t - H_0 + \mathcal{O}(\delta^2 \partial_t^3) \right] R(\vec{r}, t) = \int d^3 r' U(\vec{r}, \vec{r}') R(\vec{r}', t), \quad (4)$$

where $H_0 = -\nabla^2/(2\mu)$. $\mu = (m_M m_B)/(m_M + m_B)$ is the reduced mass of the system, and $\delta = (m_M - m_B)/(m_M + m_B)$ is a dimensionless parameter associated with the difference between the meson and baryon masses. The interaction kernel, $U(\vec{r}, \vec{r}')$, is an energy-independent non-local interaction, which ensures the unitarity of the S -matrix and manifests the correct scattering phase shifts up to the lowest inelastic threshold.

In practice, $U(\vec{r}, \vec{r}')$ is often expanded by the derivative expansion as

$$U(\vec{r}, \vec{r}') = V_{\text{LO}}(r) \delta^3(\vec{r} - \vec{r}') + \mathcal{O}(\nabla^n). \quad (5)$$

By substituting the first term of Eq. (5) into Eq. (4), we can obtain the leading-order potential $V_{\text{LO}}(r)$ from the R-correlator as

$$V_{\text{LO}}(r) = R(\vec{r}, t)^{-1} \left[\frac{1 + 3\delta^2}{8\mu} \partial_t^2 - \partial_t - H_0 \right] R(\vec{r}, t), \quad (6)$$

where we omitted terms of $\mathcal{O}(\delta^2 \partial_t^3)$. The omitted terms have been numerically checked to be insignificant for our system of interest. In this paper, we only present results of the leading-order potential $V_{\text{LO}}(r)$. Effects from the higher-order terms in the derivative expansion are found to be controlled as we investigate in Appendix C.

We then obtain the phase shifts by solving the Schrödinger equation in infinite volume

$$\left(-\frac{\nabla^2}{2\mu} + V_{\text{fit}}(r) \right) \psi(\vec{r}; E) = \frac{k^2}{2\mu} \psi(\vec{r}; E), \quad (7)$$

where $V_{\text{fit}}(r)$ is the potential function fitted to the original potential $V_{\text{LO}}(r)$ and k is the relative momentum in the center-of-mass frame that is related to the energy as $E = \sqrt{k^2 + m_M^2} + \sqrt{k^2 + m_B^2}$.

III. SETUP

In this section, we present the details of our lattice simulation. We use the following operators for the local sink operators of the \bar{D} meson and the nucleon,

$$\bar{D}_i(x) = \bar{c}(x)i\gamma_5q_i(x), \quad (8)$$

$$N_{\alpha,i}(x) = \varepsilon_{abc} \left[u^a(x)^T C \gamma_5 d^b(x) \right] q_{\alpha,i}^c(x), \quad (9)$$

where $\bar{D} = (\bar{D}^0, D^-)^T$, $N_\alpha = (p_\alpha, n_\alpha)^T$, and $q = (u, d)^T$. The indices a, b , and c denote the color indices, and α denotes the spinor index. The charge conjugation operator is given by $C = \gamma_4\gamma_2$. For the source operator, we use a wall-type operator with Coulomb gauge fixing, which enhances the overlap with the low-energy $\bar{D}N$ states.

The correlation functions are computed with the unified contraction algorithm [49], using the gauge configurations, "HAL-conf-2023", generated by the HAL QCD collaboration at the physical pion mass [44]. (2+1)-flavor non-perturbatively $\mathcal{O}(a)$ -improved Wilson quark action with stout smearing, along with the Iwasaki gauge action at a bare coupling constant of $\beta = 1.82$ is used. The size of the lattice is $L^4 = 96^4$ with a lattice spacing of $a = 0.084372(54)(^{+109}_{-6})$ fm, corresponding to an inverse lattice spacing of $a^{-1} = 2338.8(1.5)(^{+0.2}_{-3.0})$ MeV. The pion and nucleon masses are $m_\pi = 137.1(0.3)(^{+0.0}_{-0.2})$ MeV and $m_N = 939.7(1.8)(^{+0.2}_{-1.7})$ MeV, respectively. We use this fixed value of m_N for the nucleon mass in our analysis. For the charm quark action, we use the relativistic heavy-quark (RHQ) action given in Ref. [50], which eliminates discretization errors up to next-to-leading-order. Two sets of parameters for the RHQ action given in Ref. [51] are used in this study, where one set (Set-I) with a slightly heavier charm quark mass and another set (Set-II) with a slightly lighter charm quark mass compared to the physical charm quark mass. The corresponding masses of the \bar{D} (\bar{D}^*) meson in Set-I and Set-II are given in Tab. IV of Appendix A.

For statistics, we use 360 gauge configurations sampled at intervals of five trajectories. To enhance statistical precision, the correlation functions are averaged over both forward and backward propagation directions for each configuration. In addition, 96×4 measurements are performed by shifting the source operator in the temporal direction and applying four rotations for the temporal direction using the hypercubic symmetry. The total number of measurements used is thus 276,480 measurements.

Statistical uncertainties are estimated by using the jackknife sampling method. Bin size dependence was checked for cases with bin sizes of 20, 30, and 40 configurations, and it has been confirmed to be small. In this paper, we present the results where the bin size is fixed to 30 configurations.

Isospin projections onto the isospin $I = 0$ and $I = 1$ channels are performed by taking the linear combination of the 4-point correlation functions as

$$C_{4\text{pt},\alpha}^{\bar{D}N(I=0)}(\vec{r}, t) = \frac{1}{\sqrt{2}}C_{4\text{pt},\alpha}^{\bar{D}^0n}(\vec{r}, t) - \frac{1}{\sqrt{2}}C_{4\text{pt},\alpha}^{D^-p}(\vec{r}, t), \quad (10)$$

$$C_{4\text{pt},\alpha}^{\bar{D}N(I=1)}(\vec{r}, t) = \frac{1}{\sqrt{2}}C_{4\text{pt},\alpha}^{\bar{D}^0n}(\vec{r}, t) + \frac{1}{\sqrt{2}}C_{4\text{pt},\alpha}^{D^-p}(\vec{r}, t). \quad (11)$$

Also, since we will only be concerned with the s -wave component in this study, the R-correlators are projected onto the A_1^+ representation of the octahedral group \mathcal{O}_h as

$$R_{A_1^+}(\vec{r}, t) = \frac{1}{48} \sum_{g \in \mathcal{O}_h} \chi_{A_1^+}(g) R(g^{-1}\vec{r}, t), \quad (12)$$

where $\chi_{A_1^+}$ are the characters of the A_1^+ representation. To further suppress contributions from higher partial waves with orbital angular momenta of $l = 4, 6, \dots$, we apply the Misner method discussed in detail in Refs. [52, 53]. In the subsequent sections we show the results with $n_{\text{max}} = 2$, $l_{\text{max}} = 4$, and $\Delta/a = 1.0$, following the notation of Ref. [53]. The results are stable with respect to the change of n_{max} and l_{max} in the region $\Delta/a \approx 1$.

IV. INTERACTION POTENTIAL BETWEEN \bar{D} AND N

The LO potential $V_{\text{LO}}(r)$ of the $\bar{D}N$ system can be obtained by applying Eq. (6) to the R-correlators computed under our setup discussed in the previous section. In this section we show $V_{\text{LO}}(r)$ for three consecutive time slices $t/a = 13-15$. The window of time slices has been chosen where contributions from excited states at small times are suppressed while avoiding the exponentially growing statistical errors at larger times. In terms of the charm quark mass dependence, we take a weighted average of the LO potentials calculated for Set-I and Set-II, i.e., $V_{\text{LO}}(r) = w_1 V_{\text{LO}}^{(\text{Set-I})}(r) + w_2 V_{\text{LO}}^{(\text{Set-II})}(r)$ throughout the rest of the analysis, where the weights $(w_1, w_2) = (0.411, 0.589)$ are determined to linearly interpolate the \bar{D} meson masses of Set-I and Set-II to the physical (PDG) value of the \bar{D}^0 meson mass. We note that the relative difference between the LO potential obtained from Set-I and Set-II is the order of a few percent, and is much smaller relative to the statistical

uncertainties of the potential. Therefore, a linear interpolation should be an appropriate interpolation to the physical charm quark setup. For more details, see Appendix B.

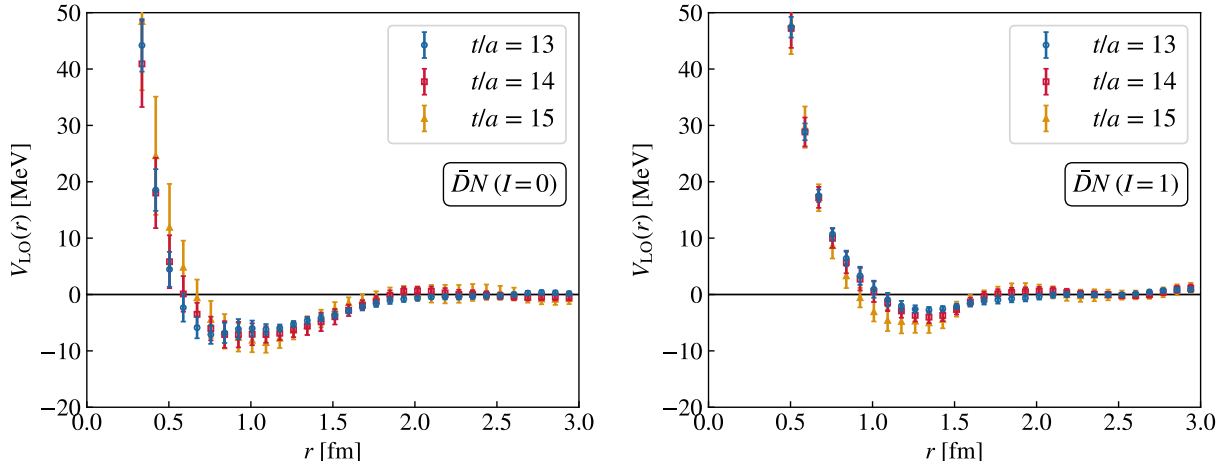


FIG. 1: LO potential $V_{\text{LO}}(r)$ for the $\bar{D}N$ system in the isospin $I = 0$ channel (left), and the $I = 1$ channel (right) at Euclidean time slices $t/a = 13$ (blue, circle), $t/a = 14$ (red, square) and $t/a = 15$ (gold, triangle).

The LO potentials $V_{\text{LO}}(r)$ for the $I = 0$ channel and the $I = 1$ channel are shown in Fig. 1. $V_{\text{LO}}(r)$ shows little time dependence within the time window of $t/a = 13-15$, indicating that contributions from excited states and the truncation error in the derivative expansion are negligible in comparison to the statistical fluctuations. We observe that $V_{\text{LO}}(r)$ has a repulsive core in the short-distance region and an attractive pocket in the intermediate-to-long-distance region for both isospin channels. For the $I = 0$ channel, $V_{\text{LO}}(r)$ has a repulsive core in the short-distance region up to around 0.5 fm and an attractive pocket between 0.5 fm to 2.0 fm. The attractive pocket has a maximum depth of about 10 MeV at around $r \simeq 1.0$ fm. For the $I = 1$ channel, $V_{\text{LO}}(r)$ has a repulsive core in the short-distance region up to around 1.0 fm and an attractive pocket between 1.0 fm to 2.0 fm. The attractive pocket has a maximum depth of a 2-5 MeV at around $r \simeq 1.2$ fm. As a general feature, the $I = 1$ channel shows stronger repulsion (or smaller attraction) compared to the $I = 0$ channel.

The LO potential can also be decomposed into isospin-independent parts and depen-

dent parts as

$$V_{\text{LO}}(r) = V_0(r) + V_\tau(r)\vec{\tau}_{\bar{D}} \cdot \vec{\tau}_N, \quad (13)$$

where $\vec{\tau}_{\bar{D}}$ ($\vec{\tau}_N$) are the isospin operators acting on the \bar{D} meson (nucleon). $V_0(r)$ and $V_\tau(r)$ can be expressed by $V_{\text{LO}}^{(I=0,1)}$ as

$$V_0(r) = \frac{1}{4}V_{\text{LO}}^{(I=0)} + \frac{3}{4}V_{\text{LO}}^{(I=1)}, \quad (14)$$

$$V_\tau(r) = -\frac{1}{4}V_{\text{LO}}^{(I=0)} + \frac{1}{4}V_{\text{LO}}^{(I=1)}. \quad (15)$$

In Fig. 2, we show $V_0(r)$ and $V_\tau(r)$ at Euclidean time slices $t/a = 13-15$. We observe that

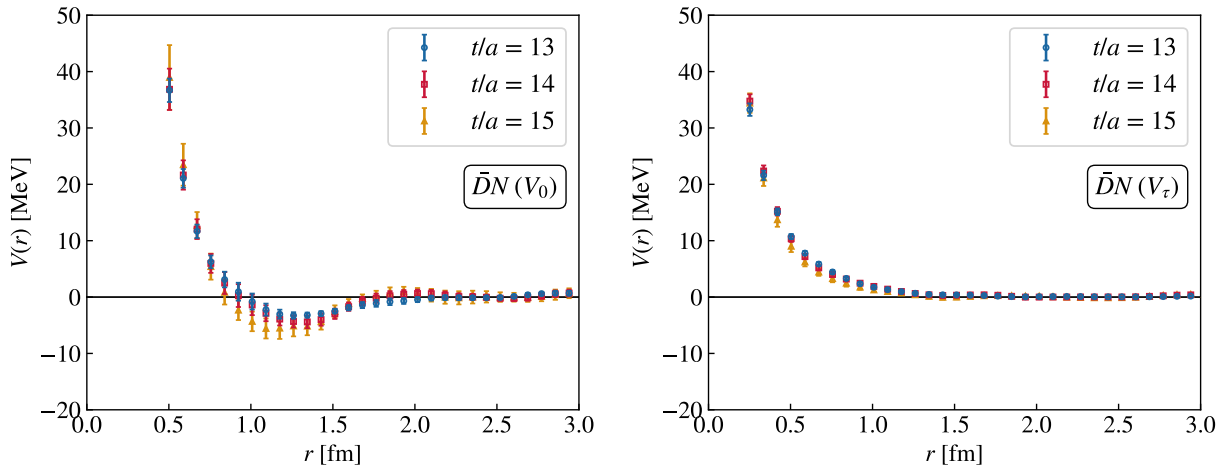


FIG. 2: Isospin independent and dependent components $V_0(r)$ and $V_\tau(r)$ at Euclidean time slices $t/a = 13$ (blue, circle), $t/a = 14$ (red, square) and $t/a = 15$ (gold, triangle).

$V_0(r)$ has an attractive pocket between $r \sim 0.8$ fm to $r \sim 2.0$ fm and $V_\tau(r)$ is positive and confined at short distances, $r \lesssim 1$ fm. In the $I = 0$ channel, $V_\tau(r)$ appears with a negative sign and acts as a totally attractive force, and for the $I = 1$ channel $V_\tau(r)$ contributes with a positive sign and acts as a purely repulsive force.

A. Comparison to KN Systems

The KN system is the strange-sector analogue of $\bar{D}N$, replacing the anti-charm quark with an anti-strange quark. In Fig. 3, we show the LO potentials of $\bar{D}N$ and KN in the $I = 0$ and $I = 1$ channels at Euclidean time slice $t/a = 14$. The KN potential, taken

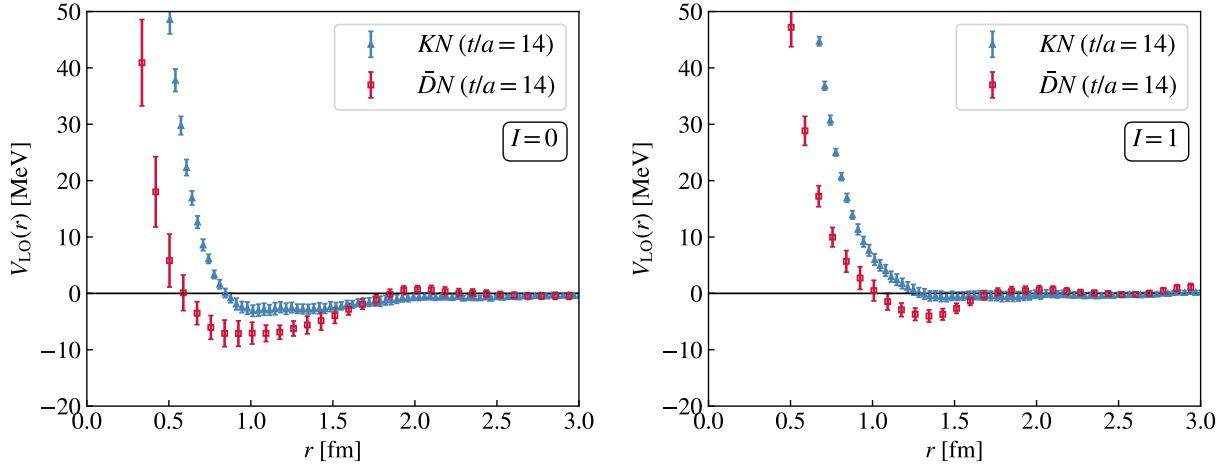


FIG. 3: $V_{LO}(r)$ for the $\bar{D}N$ system (red, square) and KN system (blue, triangle) in the isospin $I = 0$ channel (left), and the $I = 1$ channel (right) at Euclidean time slice $t/a = 14$. The KN potential is taken from Ref. [46].

from Ref. [46], was obtained by the HAL QCD method using the same lattice setup and statistics. The qualitative features are the same for other time slices, e.g., $t/a = 13$ or $t/a = 15$.

We find that the $\bar{D}N$ system manifests stronger attraction in both isospin channels than the KN system. Its repulsive core is confined to a shorter range than that of KN . In the $I = 0$ channel, the attractive pocket is deeper by approximately a factor of two compared to the KN case. Moreover, we observe a small attractive pocket in the $I = 1$ channel of $\bar{D}N$, whereas no such feature is clearly visible for KN . This may signal enhanced attraction arising from the larger $\bar{D}N$ - \bar{D}^*N channel-coupling effect which has been discussed in phenomenological models [20–23, 26]. In particular, Ref. [26] shows that meson-exchange box diagrams involving intermediate \bar{D}^* mesons provide a sizable contribution to the attraction, in contrast to the KN case where such contributions are small.

V. SCATTERING QUANTITIES OF $\bar{D}N$ SYSTEM IN s -WAVE

In this section we obtain the s -wave phase shifts, scattering length and effective range from the potential given in Section IV. To extract the s -wave phase shifts, we parameterize $V_{LO}(r)$ by two functional forms; a purely phenomenological four-Gaussian (4G) form, and

a three-Gaussian form with an additional two-pion exchange term (3G+TPE) inspired by the fact that two-pion exchange is the longest range mode since one-pion exchange is prohibited by parity conservation. The same fitting form was used for the 3G+TPE fit in the HAL QCD analysis of the KN system [46].

The parameterizations are explicitly given by

$$V_{\text{fit}}^{4\text{G}}(r) = a_1 e^{-(r/b_1)^2} + a_2 e^{-(r/b_2)^2} + a_3 e^{-(r/b_3)^2} + a_4 e^{-(r/b_4)^2}, \quad (16)$$

$$V_{\text{fit}}^{3\text{G}+\text{TPE}}(r) = c_1 e^{-(r/d_1)^2} + c_2 e^{-(r/d_2)^2} + c_3 e^{-(r/d_3)^2} + c_{\text{TPE}}(1 - e^{-\Lambda^2 r^2})^2 \frac{e^{-2m_\pi r}}{r^2}, \quad (17)$$

where $\{a_i\}$, $\{b_i\}$, $\{c_i\}$, $\{d_i\}$, c_{TPE} and Λ are real-valued fitting parameters which satisfy $b_1 < b_2 < b_3 < b_4$ and $d_1 < d_2 < d_3$, and m_π is the pion mass. $(1 - e^{-\Lambda^2 r^2})^2$ is a form factor term to regularize the two-pion exchange term at the origin. Since the systematics to the phase shift at low energies arising from the choice of the fitting form predominantly originates from the difference in the long-range region of the potential, we fix d_1 and d_2 in the 3G+TPE fit to the same values as b_1 and b_2 in the four-Gaussian fit, respectively. The fitting parameters are determined by performing an uncorrelated fit with a fitting range chosen as the interval from $r = 0$ fm to $r \simeq 4.0$ fm. For $V_{\text{LO}}(0)$, we substitute the values from the A_1^+ projected R-correlator, since the Misner method is not applicable at the origin [53]. The effect of this prescription is negligible when calculating the phase shifts in the low-energy region. The fitted parameters for the 4G fit and the 3G+TPE fit at the time slice $t/a = 14$ are listed in Tabs. I and II together with their χ^2/dof values, respectively. The chi-square values for the 3G+TPE fit are larger than the 4G fit, but are still comparable in magnitude. In Fig. 4, we show the 4G fit and 3G+TPE fit for $r^2 V_{\text{LO}}(r)$ at $t/a = 14$. We see that the 3G+TPE fit has a longer attractive tail compared to that of the 4G fit, and thus we expect larger attractive behavior in the phase shifts.

TABLE I: Fitted parameters $\{a_i\}$ and $\{b_i\}$ for the 4G fit at the time slice $t/a = 14$. Values in parentheses are the statistical uncertainties.

I	χ^2/dof	a_1 [MeV]	a_2 [MeV]	a_3 [MeV]	a_4 [MeV]	b_1 [fm]	b_2 [fm]	b_3 [fm]	b_4 [fm]
0	0.42(31)	363(47)	257(45)	292(241)	-269(264)	0.111(7)	0.227(24)	0.745(230)	0.828(148)
1	0.74(57)	725(38)	380(30)	383(118)	-307(119)	0.124(2)	0.268(11)	0.726(52)	0.777(49)

TABLE II: Fitted parameters $\{c_i\}$, $\{d_i\}$, c_{TPE} and Λ for the 3G+TPE fit at time slice $t/a = 14$. Values in parentheses are the statistical uncertainties. d_1 and d_2 are fixed to the same values as b_1 and b_2 in the 4G fit given in Tab. I, respectively.

I	χ^2/dof	c_1 [MeV]	c_2 [MeV]	c_3 [MeV]	d_3 [fm]	c_{TPE} [MeV fm ²]	Λ [MeV]
0	0.77(50)	394(70)	152(140)	100(157)	0.595(141)	-55(21)	387(271)
1	1.12(80)	717(38)	277(71)	186(82)	0.560(58)	-34(16)	509(165)

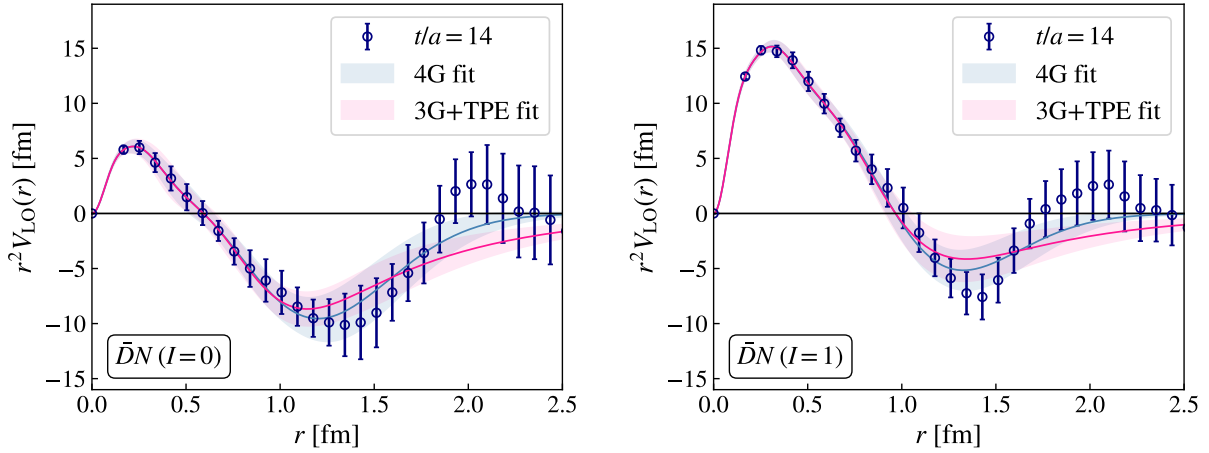


FIG. 4: $r^2 V_{\text{LO}}(r)$ for the $I = 0$ (left) and $I = 1$ channel (right) at Euclidean time slice $t/a = 14$. The blue and pink bands represent the 4G fit and the 3G+TPE fit, respectively.

We then obtain the s -wave phase shifts of $\bar{D}N$ scattering by solving Eq. (7) in the infinite volume with $V_{\text{fit}}^{4\text{G}}(r)$ and $V_{\text{fit}}^{3\text{G}+\text{TPE}}(r)$ at $t/a = 13$ -15. Phase shifts δ_0 obtained from $V_{\text{fit}}^{4\text{G}}(r)$ for $I = 0$ and $I = 1$ channels are shown in Fig. 5. We also show the comparison of the phase shifts from $V_{\text{fit}}^{4\text{G}}(r)$ and $V_{\text{fit}}^{3\text{G}+\text{TPE}}(r)$ at $t/a = 14$ in Fig. 6. The phase shifts obtained from both fits differ within the statistical uncertainties and share the same general features. The time-slice dependence of δ_0 is found to be within the statistical uncertainties. We see that δ_0 in $I = 0$ shows an attractive behavior in the low-energy region, while δ_0 in $I = 1$ shows a repulsive behavior in all energy regions. The phase shift at large momentum was numerically confirmed to converge to zero indicating $\Delta\delta = \delta_0(0) - \delta_0(\infty) = 0$. Thus from Levinson's theorem we conclude there is no bound states in both isospin channels. We also do not observe any rapid rise in the phase shift crossing $\pi/2$, indicating the absence

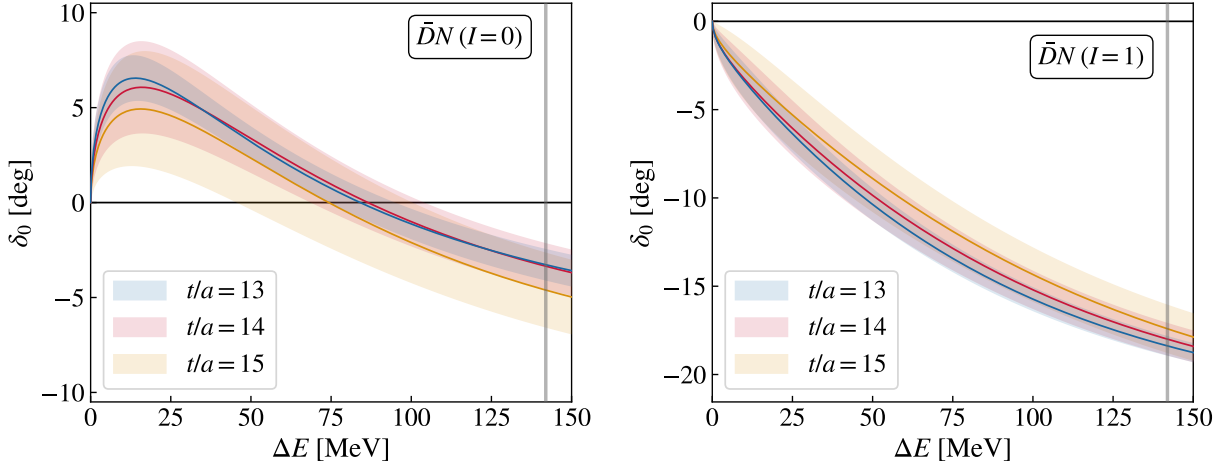


FIG. 5: s -wave phase shifts δ_0 for $I = 0$ (left), and $I = 1$ (right) channels at Euclidean times $t/a = 13$ (blue), $t/a = 14$ (red) and $t/a = 15$ (gold) from the 4G fit. $\Delta E = E - m_D - m_N$. The vertical lines at $\Delta E \simeq 140$ MeV show the inelastic threshold of \bar{D}^*N .

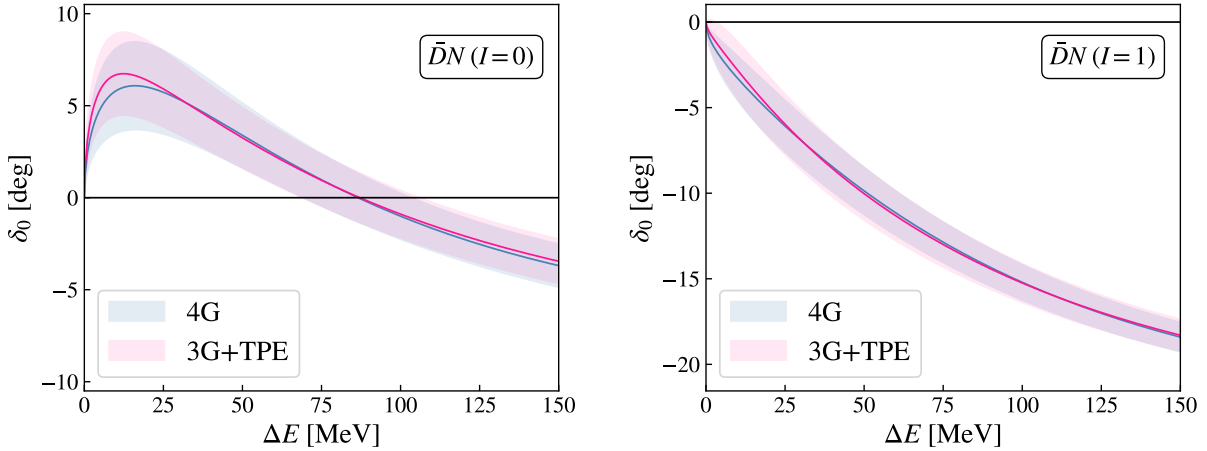


FIG. 6: s -wave phase shifts δ_0 for $I = 0$ (left) and $I = 1$ (right) channels obtained from the 4G fit (blue) and 3G+TPE fit (pink) at the Euclidean time slice $t/a = 14$. $\Delta E = E - m_D - m_N$.

of resonances near the physically accessible region of $\bar{D}N$ scattering.

When k is sufficiently small, $k \cot \delta_0$ can be expanded by the effective range expansion

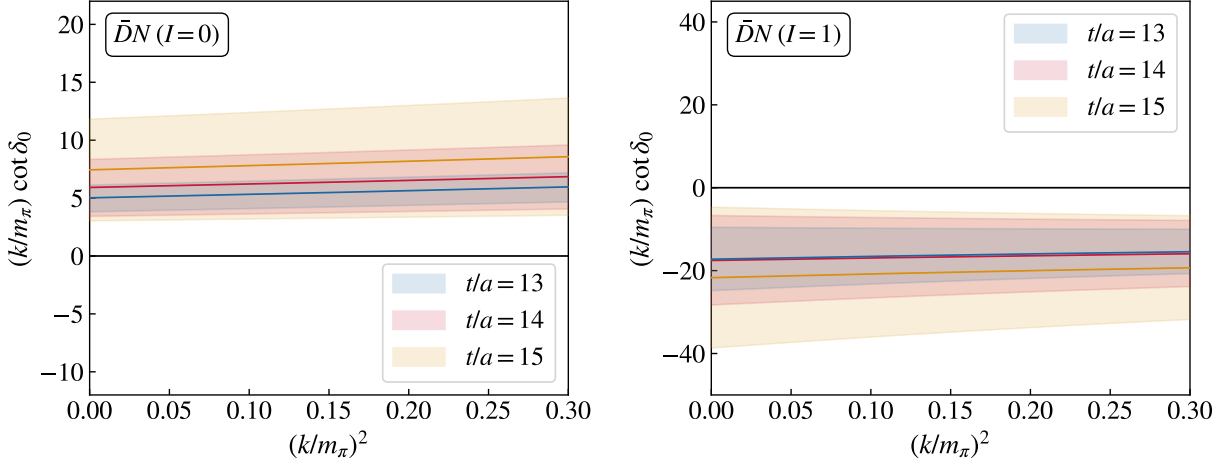


FIG. 7: $k \cot \delta_0/m_\pi$ in terms of k^2/m_π^2 for $I = 0$ (left), and $I = 1$ (right) at Euclidean times $t/a = 13$ (blue), $t/a = 14$ (red) and $t/a = 15$ (gold) from the 4G fit.

(ERE) as

$$k \cot \delta_0 = \frac{1}{a_0} + \frac{1}{2} r_{\text{eff}} k^2 + \mathcal{O}(k^4), \quad (18)$$

where a_0 (r_{eff}) is the scattering length (effective range). $k \cot \delta_0$ obtained from $V_{\text{fit}}^{4\text{G}}(r)$ for $I = 0$ and $I = 1$ channels are shown in Fig. 7 where $1/a_0$ corresponds to the intercept to the vertical axis, and r_{eff} corresponds to the slope of the line, respectively. The scattering length and effective range are determined by fitting $k \cot \delta_0$ discarding the higher-order terms of $\mathcal{O}(k^4)$ in Eq.(18). Varying the fitting range from $(k/m_\pi)^2 \in [0.00, 0.07]$ to $(k/m_\pi)^2 \in [0.00, 0.27]$, we confirm that the fitting range uncertainties in the scattering length and effective range are under control for both the 4G case and the 3G+TPE case. Using the values at $t/a = 14$ with a fitting range of $(k/m_\pi)^2 \in [0.00, 0.17]$ as center values, we obtain, $a_0^{I=0} = 0.246 \pm 0.105^{(+0.037)}_{(-0.051)}$ fm, $r_{\text{eff}}^{I=0} = 8.52 \pm 2.85^{(+2.05)}_{(-0.17)}$ fm, $a_0^{I=1} = -0.086 \pm 0.050^{(+0.015)}_{(-0.001)}$ fm and $r_{\text{eff}}^{I=1} = 13.5 \pm 29.9^{(+6.1)}_{(-0.6)}$ fm for the 4G fit case, and $a_0^{I=0} = 0.321 \pm 0.116^{(+0.026)}_{(-0.040)}$ fm, $r_{\text{eff}}^{I=0} = 9.69 \pm 3.18^{(+2.11)}_{(-0.38)}$ fm, $a_0^{I=1} = -0.052 \pm 0.071^{(+0.013)}_{(-0.002)}$ fm and $r_{\text{eff}}^{I=1} = 79.7 \pm 442.1^{(+74.9)}_{(-9.6)}$ fm for the 3G+TPE fit case, where the second and third terms are the statistical and systematic errors, respectively. The systematic errors are evaluated by considering the time-slice dependence between $t/a = 13, 15$ and $t/a = 14$, together with the ERE fit-range dependence in k . $a_0^{I=0}$ ($a_0^{I=1}$) are positive (negative) manifesting the attractive (repulsive) behavior of the $\bar{D}N$ interaction in the low-energy region.

We consider other sources of systematic errors, (i) finite volume effect of the periodic box, (ii) the interpolation to physical charm quark mass, (iii) truncation of the derivative expansion of the interaction kernel. The finite volume effect is expected to be negligible because of the large volume of the box ($L/2 = 4.06$ fm) compared to the interaction range (~ 2.0 fm). The interpolation to physical charm quark mass can be performed at different steps, for example, at the level of the R-correlators, the potentials, or the phase shifts. The associated systematic uncertainty from interpolating at different steps, however, has been confirmed to be very small ($\ll 1\%$). In order to study the truncation error of the derivative expansion, we evaluated the finite-volume energy levels from our LO potential, and compared them to the effective energy calculated directly from the R-correlators as shown in Appendix C. The ground state energy level calculated from the LO potential agrees with the effective energy, indicating that the effect from the truncation of the derivative expansion is small.

In Tab. III, we present our final results on the $\bar{D}N$ scattering length and effective range. The final systematic error is determined by taking the quadratic mean of the systematic error of the 4G fit and the difference between the 4G fit and 3G+TPE fit. We exclude the results of r_{eff} in the $I = 1$ channel since the magnitude and sign could not be well determined due to large statistical uncertainties that strongly depend on the fitting functions.

TABLE III: Scattering length and effective range of the $\bar{D}N$ system in s -wave. The second (third) term is the statistical (systematic) uncertainties.

I	a_0 [fm]	r_{eff} [fm]
0	$0.246 \pm 0.105^{(+0.084)}_{(-0.051)}$	$8.52 \pm 2.85^{(+2.36)}_{(-0.17)}$
1	$-0.086 \pm 0.050^{(+0.037)}_{(-0.001)}$	—

A. Comparison of Scattering Length to Model Studies

In Fig. 8, we show a comparison of the $\bar{D}N$ scattering lengths obtained in the present study with results from several models where the scattering lengths are available in literature. The results of the following models are presented. A model with SU(4)

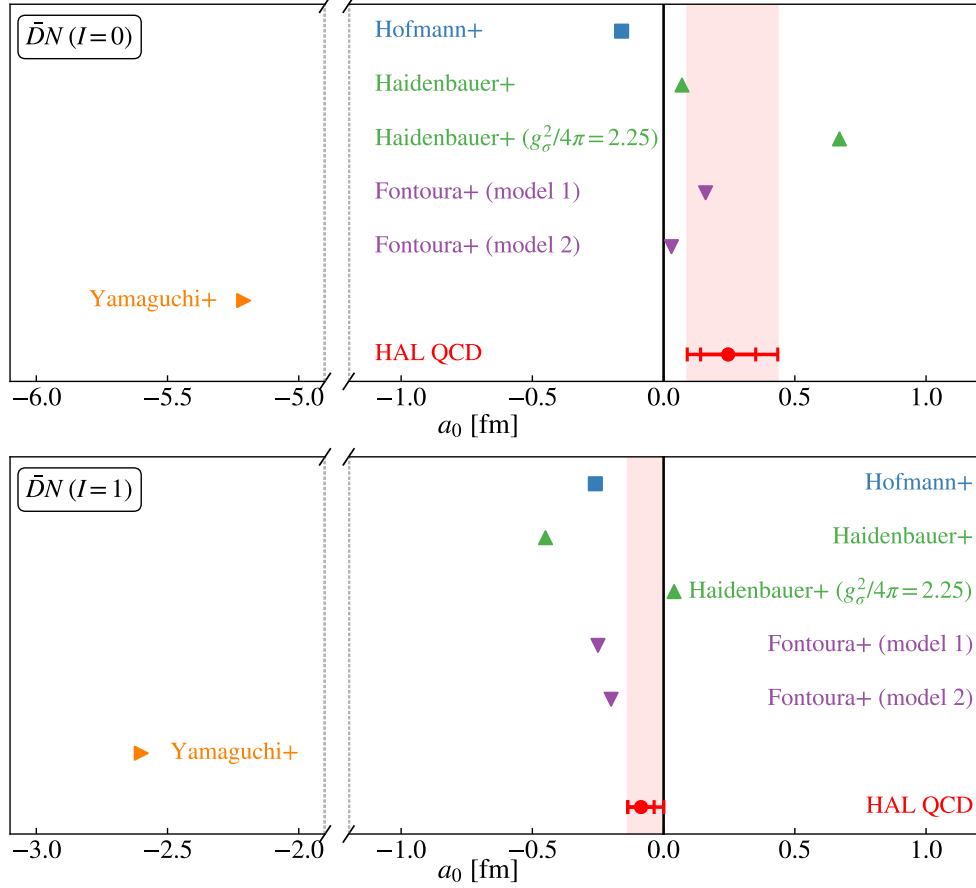


FIG. 8: Comparison of $\bar{D}N$ scattering length to model studies [23, 25, 26, 28]. The red point (and band) is our results given in Tab. III. The inner error bars represent the statistical uncertainties and the outer error bars represent the statistical and systematic uncertainties combined. "Haidenbauer+ ($g_\sigma^2/4\pi = 2.25$)" is the result from the model Ref. [26] with increased g_σ^2 where the value is given in Ref. [29].

contact interaction and vector-meson exchange [25], meson-exchange models with an explicit short-distance quark-gluon exchange interaction [26, 28] and a meson-exchange model respecting both chiral and heavy-quark spin symmetry [23]. We observe that the scattering lengths from our study are within the same order of magnitude to the model studies except for Ref. [23] which exhibits a bound state. Our results can be used to constrain model parameters and further improve theoretical models concerning the $\bar{D}N$ interaction.

VI. SUMMARY AND OUTLOOK

We study the $\bar{D}N$ scattering from lattice QCD simulations for the first time with gauge configurations generated at the physical point with a pion mass $m_\pi \simeq 137$ MeV. Using the HAL QCD method, we obtain the leading-order $\bar{D}N$ potential in the derivative expansion for the isospin $I = 0$ and $I = 1$ channels in s -wave. The $\bar{D}N$ potentials in both the $I = 0$ channel and the $I = 1$ channel manifest a repulsive core at short distances with an attractive pocket at intermediate to long distances, while the $I = 0$ channel shows stronger attraction than the $I = 1$ channel. We also compare the $\bar{D}N$ potentials to the KN potentials in Ref. [46] obtained using the same configurations, and find that $\bar{D}N$ shows stronger attraction than KN in both isospin channels. This may be a sign of the relatively larger channel-coupling effect discussed in phenomenological models [20–23, 26]. We obtain the s -wave phase shifts, scattering length and effective range from the obtained $\bar{D}N$ potentials. The s -wave phase shift of the $I = 0$ channel shows weak attraction in the low-energy region with a positive scattering length of $a_0 = 0.246 \pm 0.105^{(+0.084)}_{(-0.051)}$ fm, whereas the $I = 1$ channel shows repulsion in all energy regions with a negative scattering length of $a_0 = -0.086 \pm 0.050^{(+0.037)}_{(-0.001)}$ fm. Our study finds that the attraction between the \bar{D} meson and the nucleon is small, and therefore no s -wave bound states (pentaquark states) exist in the $I = 0$ or $I = 1$ channels of the $\bar{D}N$ system.

For future work, it would be interesting to perform a coupled-channel lattice calculation of the $\bar{D}N$ - \bar{D}^*N system and its extension to BN - B^*N system. Especially in the BN - B^*N channel, we expect that the channel-coupling effects will play a more important role in yielding stronger attraction. Another interesting study would be the s -wave scattering of \bar{D}^*N in the $I(J^P) = 0(3/2^-)$ channel, as a theoretical study [22] predicts strong attraction leading to a Feshbach resonance decaying to $\bar{D}N$ in the d -wave. In addition, applications of our $\bar{D}N$ potential to multi-nucleon systems with \bar{D} mesons, e.g., $\bar{D}NN$ systems, \bar{D} -meson nuclei systems, would be beneficial in studying possible charmed nuclei. Finally, we plan to apply our $\bar{D}N$ potential to analyze the D^-p momentum correlation function in nucleus-nucleus collisions, for which precise experimental data are expected from LHC RUN-3 by the ALICE collaboration.

ACKNOWLEDGEMENTS

The authors would like to thank the members of the HAL QCD collaboration for the enlightening discussions. Wren Yamada is grateful for the stimulating research environment at RIKEN iTHEMS. The numerical lattice QCD simulations have been performed on the supercomputer Fugaku. We thank ILDG/JLDG [54], which serves as essential infrastructure in this study. This work was partially supported by RIKEN Incentive Research Project (“Unveiling pion-exchange interactions between hadrons from first-principles lattice QCD”), Adopting Sustainable Partnerships for Innovative Research Ecosystem (ASPIRE), Grant No. JPMJAP2318, HPCI System Research Project (hp200130, hp210165, hp220174, hp220066, hp230207, hp230075, hp240213, hp240157, hp250224, hp250195), the JSPS (Grants No. JP22H00129, JP22H04917, JP23H05439, JP25K17384) “Priority Issue on Post-K computer” (Elucidation of the Fundamental Laws and Evolution of the Universe), “Program for Promoting Researches on the Supercomputer Fugaku” (Simulation for basic science: from fundamental laws of particles to creation of nuclei) and (Simulation for basic science: approaching the new quantum era) (Grants No. JPMXP1020200105, JPMXP1020230411), and Joint Institute for Computational Fundamental Science (JICFuS).

Appendix A: Effective mass of the D (D^*) meson

The effective masses of the \bar{D} (\bar{D}^*) meson in Set-I and Set-II are shown in Fig. 9. We determine their masses m_D (m_{D^*}) by fitting their two-point correlation functions using the single cosh function on the time interval of $t/a \in [23, 32]$ ($t/a \in [20, 25]$), which are given in Table IV. As seen, the \bar{D} (\bar{D}^*) meson mass in Set-I is larger than the experimental (PDG) value [55], while the \bar{D} (\bar{D}^*) meson mass in Set-II is smaller. It must be noted that the \bar{D}^* is not a stable particle at the physical pion mass and its mass should ideally be obtained from the pole position of the $\bar{D}\pi$ scattering matrix in p -wave. However the energy of lowest lying $\bar{D}\pi$ scattering state on the lattice, approximated by free-particle scattering, is $\sqrt{m_D^2 + (2\pi/L)^2} + \sqrt{m_\pi^2 + (2\pi/L)^2} = 2092$ (2066) MeV for Set-I (Set-II), which lies considerably above the \bar{D}^* mass, so that the effect of the decay is expected to be small.

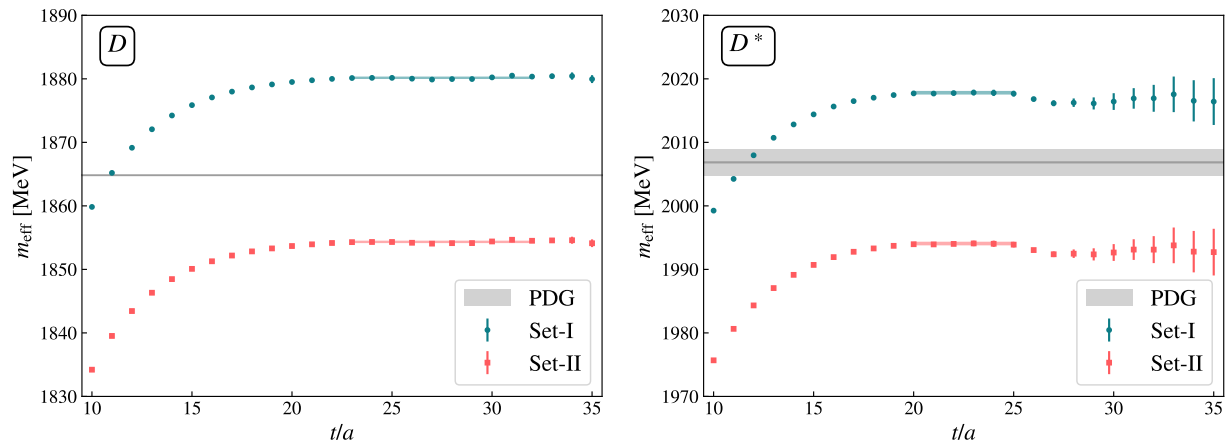


FIG. 9: Effective masses of the \bar{D} meson (left) and the \bar{D}^* meson (right) from the two-point correlation functions of Set-I and Set-II. The gray band corresponds to the PDG values [55].

TABLE IV: Masses of the \bar{D} meson and \bar{D}^* meson from Set-I and Set-II in physical units [MeV]. The values in parentheses are the statistical uncertainties. Label “Experiment” denotes the PDG values [55].

	Set-I [MeV]	Set-II [MeV]	Experiment [MeV]
m_D	1880.2 (1)	1854.3 (1)	1864.84 (5)
m_{D^*}	2017.8 (2)	1994.1 (2)	2006.85 (5)

Appendix B: Charm-quark mass dependence to the $\bar{D}N$ potential: comparison between Set-I and Set-II

As discussed in Sec. II, we used two setups for the parameters in the charm quark action. One with a slightly heavier charm quark mass (Set-I) and another with a slightly lighter charm quark mass (Set-II) compared to the physical value. Here, we compare the potentials for Set-I and Set-II, computed from their respective R-correlators using Eq. (6).

Fig. 10 shows the ratio between $V_{LO}^{(\text{Set-I})}$ and $V_{LO}^{(\text{Set-II})}$ for the time slices $t/a = 13-15$. The divergent behavior around 0.6 fm for the $I = 0$ channel and 1.0 fm for the $I = 1$ channel arises from the crossover from the repulsive part of the potential ($V_{LO} > 0$) and the attractive part ($V_{LO} < 0$). As we observe, the ratio is smaller than 1 in the repulsive

region while larger in the attractive region, showing that the potential for Set-I has a smaller repulsive core and a deeper attractive pocket compared to that of Set-II. This behavior indicates that a heavier charm quark mass yields stronger attraction near the physical charm quark mass. One possible qualitative explanation is that the larger heavy quark mass leads to a smaller mass gap between \bar{D} and \bar{D}^* (this can be seen in Tab. IV), which enhances the coupled-channel effect resulting in a larger attraction. The relative difference between $V_{\text{LO}}^{(\text{Set-I})}$ and $V_{\text{LO}}^{(\text{Set-II})}$ is rather insensitive to r and is approximately 1% which is comparable to the relative mass difference of the \bar{D} meson between Set-I and Set-II ($\sim 1\%$).

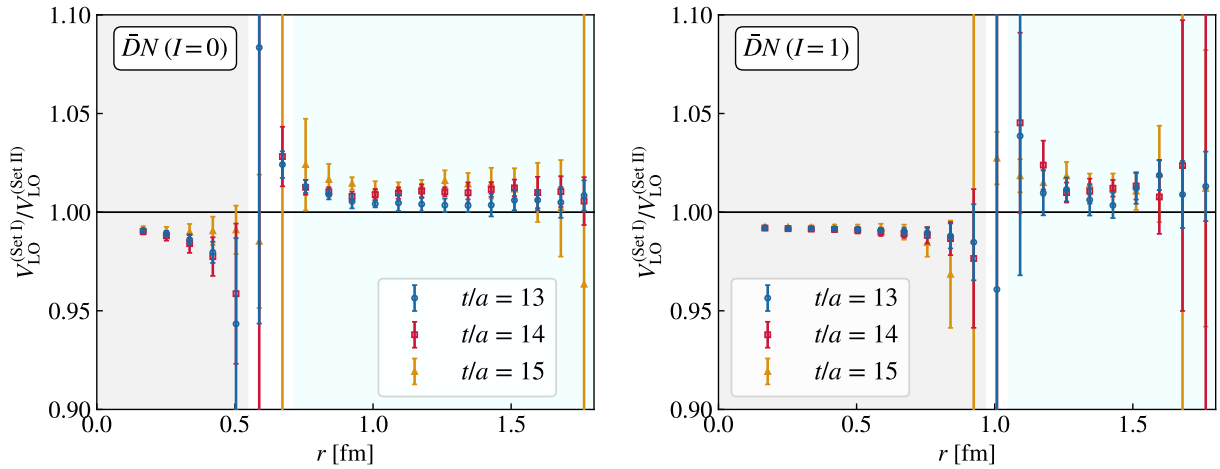


FIG. 10: Ratio of the potential $V_{\text{LO}}^{(\text{Set-I})}/V_{\text{LO}}^{(\text{Set-II})}$ obtained from Set-I and Set-II at time slices $t/a = 13$ (blue, circle), $t/a = 14$ (red, square), and $t/a = 15$ (gold, triangle) for $I = 0$ (left) and $I = 1$ (right). The gray-(cyan-) colored domains correspond the domains where

$$V_{\text{LO}} > 0 \quad (V_{\text{LO}} < 0).$$

Appendix C: Finite-volume energy levels from the HAL QCD potential and the temporal correlators

To check the systematics from the truncation in the derivative expansion, Eq. (5), we calculate the ground state energy from the leading-order HAL QCD potential in the finite three-dimensional volume, and compare it to the effective energy obtained directly from the temporal correlators. Similar analysis for different systems have been performed in

prior studies such as Refs. [46, 56, 57].

First we evaluate the ground state energy from the HAL QCD potential in a finite volume. This can be done by solving the Schrödinger equation

$$H\psi_n(\vec{r}) = \frac{k_n^2}{2\mu}\psi_n(\vec{r}), \quad (\text{C1})$$

$$H = -\frac{\nabla^2}{2\mu} + V(r),$$

in a three-dimensional box under a periodic boundary condition. Here we take $V(r)$ to be $V_{\text{LO}}(r)$ at the time slice $t/a = 14$. The eigen energies ΔE_n in the A_1^+ representation with a box size $L^3 = 96^3$ are given in Tab. V.

TABLE V: Finite volume eigen energies ΔE_n ($n = 0, 1, 2$) in the A_1^+ representation with a box size $L^3 = 96^3$ calculated from $V_{\text{LO}}(r)$ at the time slice $t/a = 14$.

	ΔE_0 [MeV]	ΔE_1 [MeV]	ΔE_2 [MeV]
$I = 0$	-0.026(300)	18.2(4)	36.7(6)
$I = 1$	0.199(337)	19.4(4)	38.5(4)

Next we evaluate the effective energy $E_0^{\text{eff}}(t)$ from the temporal correlation functions. We prepare two temporal correlation functions,

$$R(t) = \sum_{\vec{x}} R(\vec{x}, t), \quad (\text{C2})$$

$$R^{\text{opt}}(t) = \sum_{\vec{x}} \psi_0^\dagger(\vec{x}) R(\vec{x}, t), \quad (\text{C3})$$

where $R(\vec{x}, t)$ is the R-correlator defined in Eq. (3), and ψ_0 is the ground state solution of Eq. (C1). R^{opt} is projected by the ground state of the HAL QCD potential, and is expected to be optimized so that it has a dominant overlap to the actual ground state. Here we use the linearly-interpolated R-correlator from Set-I and Set-II defined as

$$R(\vec{x}, t) = w_1 R^{(\text{Set-I})}(\vec{x}, t) + w_2 R^{(\text{Set-II})}(\vec{x}, t), \quad (\text{C4})$$

with the same weights used to interpolate the potential in Sec. IV, i.e., $w_1 = 0.411$ and $w_2 = 0.589$. The effective energy is defined as

$$\Delta E_0^{\text{eff}}(t) = \frac{1}{a} \log \left[\frac{R^{(\text{opt})}(t)}{R^{(\text{opt})}(t+1)} \right]. \quad (\text{C5})$$

For sufficiently large t , $\Delta E_0^{\text{eff}}(t)$ should have a plateau at energy ΔE_0 which is the ground state energy measured from the $\bar{D}N$ threshold.

In Fig. 11, we show the effective energies obtained from the correlators, $R(t)$ and $R^{\text{opt}}(t)$, together with the ground state energies obtained from the HAL QCD potential at the time slice $t/a = 14$. The effective energies from $R(t)$ and $R^{\text{opt}}(t)$ are almost identical, indicating that the R-corralator $R(t)$ dominantly overlaps with the ground state. We also observe that the ground state energies from the LO potential coincide with the effective energies from the R-correlators within statistical fluctuations for large times $t/a = 13-15$ in both isospin channels. This indicates that the systematics arising from the leading-order truncation of the interaction kernel in the HAL QCD method is under control at low energies for the $\bar{D}N$ system.

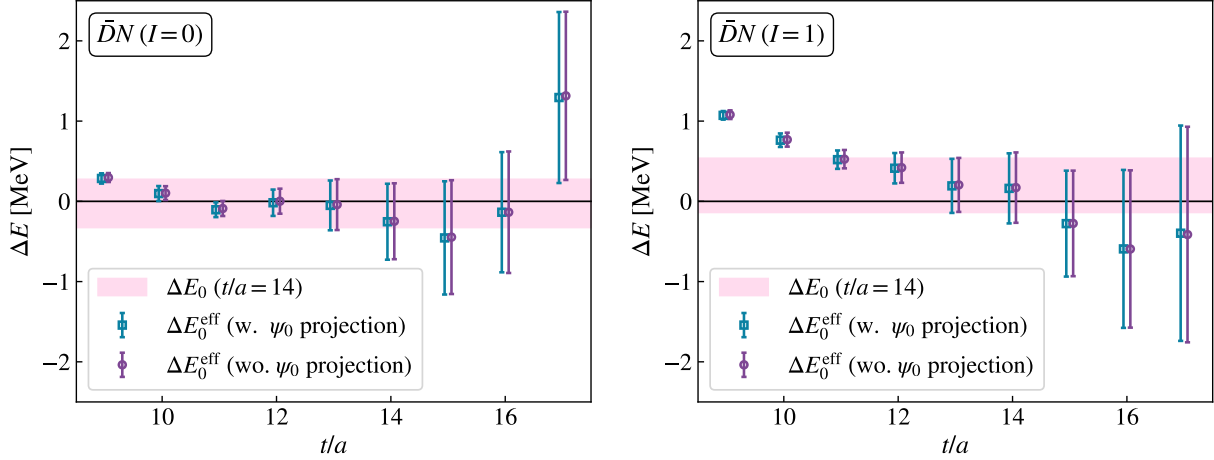


FIG. 11: Effective energies ΔE_0^{eff} from correlators $R(t)$ (purple) and $R^{\text{opt}}(t)$ (blue), and the ground state energy ΔE_0 from $V_{\text{LO}}(r)$ at $t/a = 14$ (pink band) for channels $I = 0$ (left) and $I = 1$ (right).

-
- [1] H.-X. Chen, W. Chen, X. Liu, and S.-L. Zhu, The hidden-charm pentaquark and tetraquark states, *Phys. Rept.* **639**, 1 (2016), arXiv:1601.02092 [hep-ph].
- [2] A. Hosaka, T. Iijima, K. Miyabayashi, Y. Sakai, and S. Yasui, Exotic hadrons with heavy flavors: X, Y, Z, and related states, *PTEP* **2016**, 062C01 (2016), arXiv:1603.09229 [hep-ph].

- [3] R. F. Lebed, R. E. Mitchell, and E. S. Swanson, Heavy-Quark QCD Exotica, *Prog. Part. Nucl. Phys.* **93**, 143 (2017), arXiv:1610.04528 [hep-ph].
- [4] A. Esposito, A. Pilloni, and A. D. Polosa, Multiquark Resonances, *Phys. Rept.* **668**, 1 (2017), arXiv:1611.07920 [hep-ph].
- [5] F.-K. Guo, C. Hanhart, U.-G. Meißner, Q. Wang, Q. Zhao, and B.-S. Zou, Hadronic molecules, *Rev. Mod. Phys.* **90**, 015004 (2018), [Erratum: *Rev.Mod.Phys.* 94, 029901 (2022)], arXiv:1705.00141 [hep-ph].
- [6] A. Ali, J. S. Lange, and S. Stone, Exotics: Heavy Pentaquarks and Tetraquarks, *Prog. Part. Nucl. Phys.* **97**, 123 (2017), arXiv:1706.00610 [hep-ph].
- [7] S. L. Olsen, T. Skwarnicki, and D. Zieminska, Nonstandard heavy mesons and baryons: Experimental evidence, *Rev. Mod. Phys.* **90**, 015003 (2018), arXiv:1708.04012 [hep-ph].
- [8] M. Karliner, J. L. Rosner, and T. Skwarnicki, Multiquark States, *Ann. Rev. Nucl. Part. Sci.* **68**, 17 (2018), arXiv:1711.10626 [hep-ph].
- [9] Y.-R. Liu, H.-X. Chen, W. Chen, X. Liu, and S.-L. Zhu, Pentaquark and Tetraquark states, *Prog. Part. Nucl. Phys.* **107**, 237 (2019), arXiv:1903.11976 [hep-ph].
- [10] N. Brambilla, S. Eidelman, C. Hanhart, A. Nefediev, C.-P. Shen, C. E. Thomas, A. Vairo, and C.-Z. Yuan, The *XYZ* states: experimental and theoretical status and perspectives, *Phys. Rept.* **873**, 1 (2020), arXiv:1907.07583 [hep-ex].
- [11] H.-X. Chen, W. Chen, X. Liu, Y.-R. Liu, and S.-L. Zhu, An updated review of the new hadron states, *Rept. Prog. Phys.* **86**, 026201 (2023), arXiv:2204.02649 [hep-ph].
- [12] A. Hosaka, T. Hyodo, K. Sudoh, Y. Yamaguchi, and S. Yasui, Heavy Hadrons in Nuclear Matter, *Prog. Part. Nucl. Phys.* **96**, 88 (2017), arXiv:1606.08685 [hep-ph].
- [13] G. Krein, A. W. Thomas, and K. Tsushima, Nuclear-bound quarkonia and heavy-flavor hadrons, *Prog. Part. Nucl. Phys.* **100**, 161 (2018), arXiv:1706.02688 [hep-ph].
- [14] S. J. Brodsky, I. A. Schmidt, and G. F. de Teramond, NUCLEAR BOUND QUARKONIUM, *Phys. Rev. Lett.* **64**, 1011 (1990).
- [15] K. Tsushima, D.-H. Lu, A. W. Thomas, K. Saito, and R. H. Landau, Charmed mesic nuclei, *Phys. Rev. C* **59**, 2824 (1999), arXiv:nucl-th/9810016.
- [16] A. Hayashigaki, J / psi nucleon scattering length and in-medium mass shift of J / psi in QCD sum rule analysis, *Prog. Theor. Phys.* **101**, 923 (1999), arXiv:nucl-th/9811092.
- [17] A. Hayashigaki, Mass modification of D meson at finite density in QCD sum rule, *Phys. Lett.*

- B **487**, 96 (2000), arXiv:nucl-th/0001051.
- [18] L. Tolos, J. Schaffner-Bielich, and A. Mishra, Properties of D-mesons in nuclear matter within a self-consistent coupled-channel approach, *Phys. Rev. C* **70**, 025203 (2004), arXiv:nucl-th/0404064.
- [19] M. F. M. Lutz and C. L. Korpa, Open-charm systems in cold nuclear matter, *Phys. Lett. B* **633**, 43 (2006), arXiv:nucl-th/0510006.
- [20] S. Yasui and K. Sudoh, Exotic nuclei with open heavy flavor mesons, *Phys. Rev. D* **80**, 034008 (2009), arXiv:0906.1452 [hep-ph].
- [21] D. Gamermann, C. Garcia-Recio, J. Nieves, L. L. Salcedo, and L. Tolos, Exotic dynamically generated baryons with negative charm quantum number, *Phys. Rev. D* **81**, 094016 (2010), arXiv:1002.2763 [hep-ph].
- [22] Y. Yamaguchi, S. Ohkoda, S. Yasui, and A. Hosaka, Exotic baryons from a heavy meson and a nucleon – Negative parity states –, *Phys. Rev. D* **84**, 014032 (2011), arXiv:1105.0734 [hep-ph].
- [23] Y. Yamaguchi, S. Yasui, and A. Hosaka, Open charm and bottom meson-nucleon potentials à la the nuclear force, *Phys. Rev. D* **106**, 094001 (2022), arXiv:2206.01921 [hep-ph].
- [24] N. Isgur and M. B. Wise, Weak Decays of Heavy Mesons in the Static Quark Approximation, *Phys. Lett. B* **232**, 113 (1989).
- [25] J. Hofmann and M. F. M. Lutz, Coupled-channel study of crypto-exotic baryons with charm, *Nucl. Phys. A* **763**, 90 (2005), arXiv:hep-ph/0507071.
- [26] J. Haidenbauer, G. Krein, U.-G. Meissner, and A. Sibirtsev, Anti-D N interaction from meson-exchange and quark-gluon dynamics, *Eur. Phys. J. A* **33**, 107 (2007), arXiv:0704.3668 [nucl-th].
- [27] T. F. Carames and A. Valcarce, $N\bar{D}$ system: A challenge for PANDA, *Phys. Rev. D* **85**, 094017 (2012), arXiv:1204.5502 [hep-ph].
- [28] C. E. Fontoura, G. Krein, and V. E. Vizcarra, $\bar{D}N$ interaction in a color-confining chiral quark model, *Phys. Rev. C* **87**, 025206 (2013), arXiv:1208.4058 [nucl-th].
- [29] S. Acharya et al. (ALICE), First study of the two-body scattering involving charm hadrons, *Phys. Rev. D* **106**, 052010 (2022), arXiv:2201.05352 [nucl-ex].
- [30] N. Ishii, S. Aoki, and T. Hatsuda, The Nuclear Force from Lattice QCD, *Phys. Rev. Lett.* **99**, 022001 (2007), arXiv:nucl-th/0611096.
- [31] S. Aoki, T. Hatsuda, and N. Ishii, Theoretical Foundation of the Nuclear Force in QCD and its applications to Central and Tensor Forces in Quenched Lattice QCD Simulations, *Prog.*

- Theor. Phys. **123**, 89 (2010), arXiv:0909.5585 [hep-lat].
- [32] N. Ishii, S. Aoki, T. Doi, T. Hatsuda, Y. Ikeda, T. Inoue, K. Murano, H. Nemura, and K. Sasaki (HAL QCD), Hadron–hadron interactions from imaginary-time Nambu–Bethe–Salpeter wave function on the lattice, Phys. Lett. B **712**, 437 (2012), arXiv:1203.3642 [hep-lat].
- [33] S. Aoki, T. Doi, T. Hatsuda, Y. Ikeda, T. Inoue, N. Ishii, K. Murano, H. Nemura, and K. Sasaki (HAL QCD), Lattice QCD approach to Nuclear Physics, PTEP **2012**, 01A105 (2012), arXiv:1206.5088 [hep-lat].
- [34] M. Luscher, Volume Dependence of the Energy Spectrum in Massive Quantum Field Theories. 2. Scattering States, Commun. Math. Phys. **105**, 153 (1986).
- [35] M. Luscher, Two particle states on a torus and their relation to the scattering matrix, Nucl. Phys. B **354**, 531 (1991).
- [36] T. Doi et al., Baryon interactions from lattice QCD with physical quark masses – Nuclear forces and $\Xi\Xi$ forces –, EPJ Web Conf. **175**, 05009 (2018), arXiv:1711.01952 [hep-lat].
- [37] S. Gongyo et al., Most Strange Dibaryon from Lattice QCD, Phys. Rev. Lett. **120**, 212001 (2018), arXiv:1709.00654 [hep-lat].
- [38] T. Iritani et al. (HAL QCD), $N\Omega$ dibaryon from lattice QCD near the physical point, Phys. Lett. B **792**, 284 (2019), arXiv:1810.03416 [hep-lat].
- [39] K. Sasaki et al. (HAL QCD), $\Lambda\Lambda$ and $N\Xi$ interactions from lattice QCD near the physical point, Nucl. Phys. A **998**, 121737 (2020), arXiv:1912.08630 [hep-lat].
- [40] Y. Lyu, H. Tong, T. Sugiura, S. Aoki, T. Doi, T. Hatsuda, J. Meng, and T. Miyamoto, Dibaryon with Highest Charm Number near Unitarity from Lattice QCD, Phys. Rev. Lett. **127**, 072003 (2021), arXiv:2102.00181 [hep-lat].
- [41] Y. Lyu, T. Doi, T. Hatsuda, Y. Ikeda, J. Meng, K. Sasaki, and T. Sugiura, Attractive $N-\phi$ interaction and two-pion tail from lattice QCD near physical point, Phys. Rev. D **106**, 074507 (2022), arXiv:2205.10544 [hep-lat].
- [42] Y. Lyu, S. Aoki, T. Doi, T. Hatsuda, Y. Ikeda, and J. Meng, Doubly Charmed Tetraquark T_{cc}^+ from Lattice QCD near Physical Point, Phys. Rev. Lett. **131**, 161901 (2023), arXiv:2302.04505 [hep-lat].
- [43] Y. Lyu, T. Doi, T. Hatsuda, and T. Sugiura, Nucleon-charmonium interactions from lattice QCD, Phys. Lett. B **860**, 139178 (2025), arXiv:2410.22755 [hep-lat].
- [44] T. Aoyama, T. M. Doi, T. Doi, E. Itou, Y. Lyu, K. Murakami, and T. Sugiura (HAL QCD), Scale

- setting and hadronic properties in the light quark sector with (2+1)-flavor Wilson fermions at the physical point, *Phys. Rev. D* **110**, 094502 (2024), arXiv:2406.16665 [hep-lat].
- [45] L. Zhang, T. Doi, Y. Lyu, T. Hatsuda, and Y.-G. Ma, Probing nucleon- Ω ccc interaction via lattice QCD at physical quark masses, *Phys. Lett. B* **871**, 139998 (2025), arXiv:2508.10388 [hep-lat].
- [46] K. Murakami, S. Aoki, T. Doi, Y. Lyu, and W. Yamada, S -wave kaon-nucleon interactions from lattice QCD on the physical point (2025), arXiv:2509.00838 [hep-lat].
- [47] T. Miyamoto et al., $\Lambda_c N$ interaction from lattice QCD and its application to Λ_c hypernuclei, *Nucl. Phys. A* **971**, 113 (2018), arXiv:1710.05545 [hep-lat].
- [48] K. Murakami, Y. Akahoshi, and S. Aoki (LATTICE-HALQCD), S -wave kaon-nucleon potentials with all-to-all propagators in the HAL QCD method, *PTEP* **2020**, 093B03 (2020), arXiv:2006.01383 [hep-lat].
- [49] T. Doi and M. G. Endres, Unified contraction algorithm for multi-baryon correlators on the lattice, *Comput. Phys. Commun.* **184**, 117 (2013), arXiv:1205.0585 [hep-lat].
- [50] S. Aoki, Y. Kuramashi, and S.-i. Tominaga, Relativistic heavy quarks on the lattice, *Prog. Theor. Phys.* **109**, 383 (2003), arXiv:hep-lat/0107009.
- [51] Y. Namekawa, Charm physics by $N_f = 2 + 1$ Iwasaki gauge and the six stout smeared $O(a)$ -improved Wilson quark actions on a 96^4 lattice, *PoS LATTICE2016*, 125 (2017).
- [52] C. W. Misner, Spherical harmonic decomposition on a cubic grid, *Class. Quant. Grav.* **21**, S243 (2004), arXiv:gr-qc/9910044.
- [53] T. Miyamoto, Y. Akahoshi, S. Aoki, T. Aoyama, T. Doi, S. Gongyo, and K. Sasaki, Partial wave decomposition on the lattice and its applications to the HAL QCD method, *Phys. Rev. D* **101**, 074514 (2020), arXiv:1906.01987 [hep-lat].
- [54] <http://www.lqcd.org/ildg>, <http://www.jldg.org>.
- [55] S. Navas et al. (Particle Data Group), Review of particle physics, *Phys. Rev. D* **110**, 030001 (2024).
- [56] T. Iritani, S. Aoki, T. Doi, T. Hatsuda, Y. Ikeda, T. Inoue, N. Ishii, H. Nemura, and K. Sasaki (HAL QCD), Consistency between Lüscher's finite volume method and HAL QCD method for two-baryon systems in lattice QCD, *JHEP* **03**, 007, arXiv:1812.08539 [hep-lat].
- [57] Y. Lyu, H. Tong, T. Sugiura, S. Aoki, T. Doi, T. Hatsuda, J. Meng, and T. Miyamoto, Optimized two-baryon operators in lattice QCD, *Phys. Rev. D* **105**, 074512 (2022), arXiv:2201.02782 [hep-lat].